Attosecond time-resolved electron dynamics in the hydrogen molecule

G. Sansone[1,2*], F. Kelkensberg[3], F. Morales[4,5], J. F. Pérez-Torres[4], F. Martín[4], M. J. J. Vrakking[3,5]

***Abstract*—Recent advances in the generation and characterization of XUV pulses, generated either by intense femtosecond lasers or by free electron lasers, are pushing the frontier of time-resolved investigations down to the attosecond domain, the relevant timescale for electron motion. The quantum nature of the intertwined electronic and nuclear motion requires theoretical models going beyond the Born-Oppenheimer approximation and taking into account electron correlation, representing a challenge for the computational power available nowadays. Understanding how the electron dynamics inside molecules can influence chemical reactions present important implications in several fields and allow for the development of new technologies. In this manuscript, we report on experimental and theoretical results of an investigation in H_2/D_2, where for the first time control of molecular dynamics with attosecond resolution was achieved. The data represent the first evidence of the control of the electron motion in a molecule undergoing a chemical reaction on the sub-femtosecond scale.**

I. Introduction

Understanding the inner working of molecular systems is an incredible challenging task due to the different interactions and the large number of degree of freedoms that must be considered in order to completely describe even the smallest molecule. One of the main scientific interests is the possibility to image the structural modification of molecules undergoing a chemical reaction and the possibility to control the reaction pathway. Different imaging techniques can be implemented depending on whether information about the nuclear positions or characterization of the structure and energies of valence electrons are required. Application of femtosecond visible/infrared (IR) lasers allows to initiate and resolve in time chemical reactions in different kind of molecular systems, ranging from the fastest vibrational motion taking place in H_2^+/D_2^+ [1] up to the motion of complex biomolecules [2]. The quest for imaging techniques able to freeze in time the motion of complex bio-molecules has motivated the development X-ray free electrons lasers for diffraction imaging [3]; meanwhile, extreme-ultraviolet (XUV) radiation, generated by high order harmonic generation, has been exploited as a probe to characterize the valence structure of a dissociating Br_2 molecule [4].

The generation and characterization over the last decade of attosecond pulses [5], [6], has opened new scenarios for the control of ultrafast molecular dynamics as they could allow steering of the electron motion inside complex molecular system. As the electron density distribution determines the potential energy surfaces along which the nuclear motion evolves, this could ultimately allow for the control of chemical reactions with an unprecedent temporal resolution. The relevance for an electronic timescale in chemical reaction has been suggested in theoretical works describing the response of complex molecules to photoionization [7]. These works have questioned the possibility to treat independently nuclear and electronic degrees of freedoms which is the basis of the Born-Oppenheimer approximation. This approximation reveals itself inapplicable also in other situations that are often encountered in molecular dynamics such as conical intersections where the energy difference between electronic potential surfaces along a suitable reaction coordinate goes to zero and the electron dynamics cannot be longer considered faster than the nuclear dynamics [8]. Moreover in the case of autoionization processes [9] or relaxation mechanisms taking place in clusters due to electron correlations, the nuclear dynamics cannot be treated independently from the electronic one [10]. New approaches will be required to describe processes characterized by intertwined nuclear and electronic dynamics that cannot be treated separately [11].

In this work we will present experimental data and a theoretical analysis of the first application of isolated attosecond pulses to control electronic motion in H_2/D_2 molecules. In section II the pump-probe experimental setup will be presented. The main experimental results and the general theoretical framework for controlling electron localization in dissociating molecular ions H_2^+/D_2^+ will be discussed in section III. A semiclassical model describing the electron localization processes will be presented in section IV; finally in section V a numerical model based on solution of the 3D 2-electrons Schrödinger equation beyond the Born-Oppenheimer approximation will be introduced and discussed.

II. Experimental setup

Electronic excitation or photoionization of molecules lead to nuclear motion that evolves on a typical timescale in the femtosecond regime and that depends on the mass of the nuclei involved. The nuclear motion during the excitation/ionization processes can be neglected is suitable ultrashort XUV pulses are used to initiate the molecular dynamics; in the case

1) CNR-IFN Dipartimento di Fisica Politecnico Milano Piazza Leonardo da Vinci 32 20133 Milano Italy
2) Max Planck Institut für Kernphysik Saupfercheckweg 1 69117 Heidelberg Germany
3) FOM Institute AMOLF, Science Park 104, 1098 XG Amsterdam, The Netherlands
4) Departamento de Química, C-9, Universidad Autónoma de Madrid, 28049 Madrid, Spain
5) Max-Born-Institut, Max-Born Strasse 2A, D-12489 Berlin, Germany
* giuseppe.sansone@polimi.it

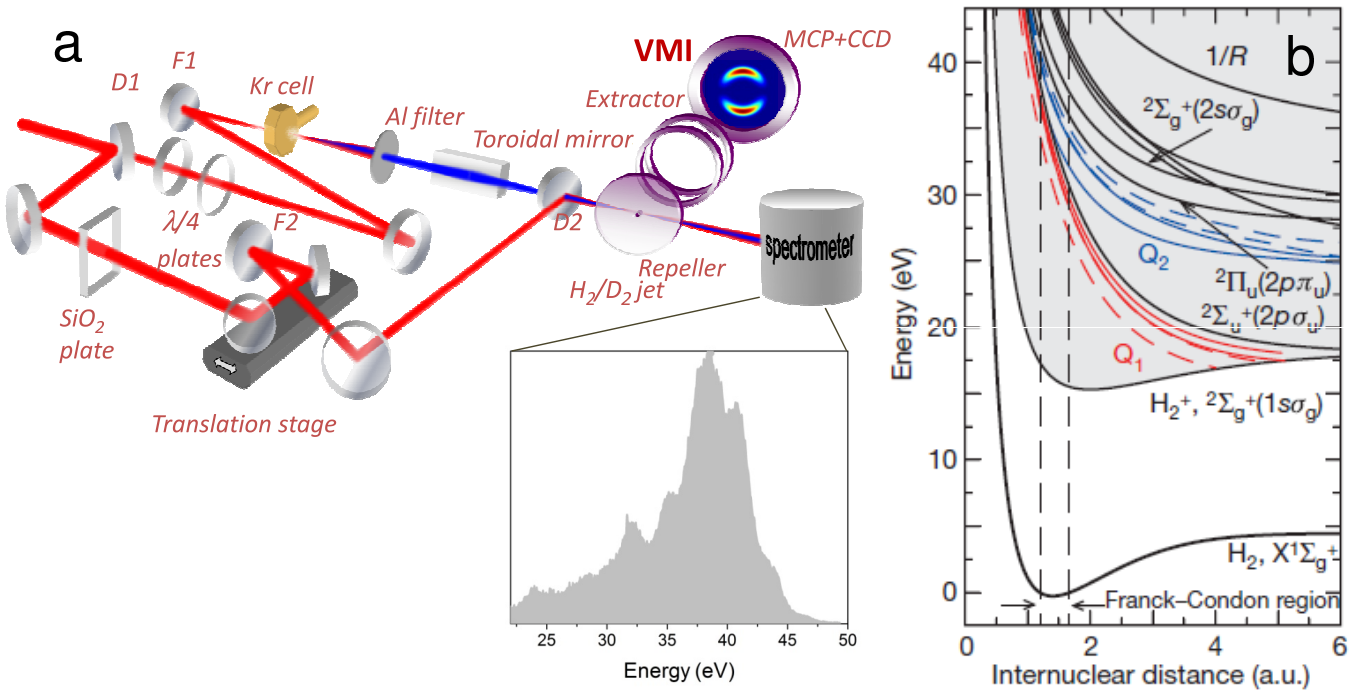

Fig. 1. a) Experimental setup used for the pump-probe experiment in H_2/D_2. D1, D2 drilled mirrors; F1 (f=25 cm), F2 (f=32 cm) spherical mirrors. Inset: typical XUV continuum generated in Krypton. b) Relevant energy levels of the molecule H_2/D_2 and of the molecular ion H_2^+/D_2^+.

of H_2/D_2, that presents a typical timescale for the nuclear motion of few-femtoseconds, sub-fs pulses as pump pulses are required. The process of high-order harmonic generation in gases leads to the formation of a train of attosecond bursts of light spaced by half-optical cycle of the driving pulse; selection of an isolated attosecond pulse from such a train can be accomplished by reducing the duration of the driving pulse down to the few-cycle regime and by modulating in time the polarization state, ensuring only a short central window of linear polarization with a duration shorter than half-optical cycle. Indeed as the HHG efficiency strongly decreases upon increasing the ellipticity of the driving pulses, only in the window of linear polarization, XUV light can be generated efficiently, leading to the emission of a single burst of XUV light. this concept is usually referred to as Polarization Gating and has been used for the generation of 130 as pulses [12]. The experimental setup used is shown in Fig. 1a: 6 fs, CEP-stable pulses, delivered by a hollow fiber compressor, were split using a drilled mirror with an aperture of 5 mm (D1). The polarization state of the beam transmitted through the mirror was modulated in time using two birefringent plates: the first 192-μm-thick quartz plate introduced a delay of $\delta = 6.2$ fs between two components propagating along the ordinary and extraordinary axes. The second plate was a zero-order quarter wave plate oriented parallel to the initial polarization direction; at the output of the second plate the polarization of the pulse was circular on the falling and leading edges with opposite helicities, and linear in the center. Considering that for a threshold ellipticity $\varepsilon_{\rm thr}$ = 0.13 the harmonic yield is reduced by a factor 2 with respect to the linear polarization case [13], the gate width τ_g can be estimated as [14]:

$$\tau_g = \frac{\varepsilon_{\rm thr}\Delta t^2}{(\ln 2)\delta} \simeq 1.09 \quad \text{fs} \tag{1}$$

with Δt initial pulse duration. For suitable Carrier-Envelope Phases (CEPs), generation of an XUV continuum, corresponding to an isolated attosecond pulse, was observed [12]. In order to generate these XUV pulses, the polarization-tailored IR pulses were focused in a 3-mm-long gas cell. In the gas cell Krypton was used as the generating medium in order to tune the photon energies of the XUV pulse to be able to reach directly the first excited state in the molecular ion

($2p\sigma_u$) but to reduce the involvement of higher lying states in the experiment as much as possible. The latter is required to effectively populate the dissociative level after $2p\sigma_u$ of the molecular ion. The XUV spectrum was filtered using a 100 nm Al filter that eliminate the IR radiation and also provided partial compensation of the intrinsic positive chirp associated with the XUV radiation. The typical spectrum measured by the XUV spectrometer is shown in the inset of Fig. 1b; the energy content covered the $1s\sigma_g$, $2p\sigma_u$ and $2p\pi_u$ states of the molecular ion and the doubly excited states Q_1 and Q_2 of the neutral molecule (see Fig. 1b). The annular part (probe pulse), reflected by a drilled mirror (D1), was delayed using a piezo-electric translation stage. Additional fused silica (SiO_2) plates were introduced in the beam path to compensate the dispersion introduced by the two birefringent plates on the other arm of the interferometer. In this way the negative chirp of the incoming pulse is compensated both in the high harmonic generation arm (harmonic cell) and in the probe arm. The probe beam was then focused using a spherical mirror (F2) and recombined collinearly with the XUV radiation by a second drilled mirror (D2). Spatial and temporal overlap between the two pulses was performed by imaging the common focal spot outside the vacuum system. The intensities of the attosecond and IR pulses in the focus were estimated in $I_{XUV} \simeq 10^9 W/cm^2$ and $I_{IR} \simeq 3-6\times 10^{12} W/cm^2$, respectively. At this common focal spot, the gas jet of a Velocity Map Imaging (VMI) spectrometer was placed. The VMI consisted of a repeller, an extractor and a drift region. The photoelectron/ion signals were acquired using an MCP coupled to a phosphor screen. The VMI allows to measure a 2D- projection of the 3D-momentum distribution of ions or electrons; under suitable approximations the original distribution can be retrieved. When running the experiment, on-line observation of the XUV spectrum was performed using an XUV spectrometer ensuring good stability of the characteristics of the XUV spectrum over extended acquisition times (typically several hours).

III. Experimental results

The 2D momentum distribution of D^+ ions generated by the XUV pulse is shown in Fig. 2a. The angular distribution is characterized by a strong signal at low energy (central part) that can be attributed to dissociation from the $1s\sigma_g$ channel, as shown in Fig. 3a, that shows the ion kinetic energy distribution generated by the XUV pulse only. Indeed all energy components above 18.1 eV (see Fig. 1b) can ionize the D_2 molecule creating a nuclear wave-packet on the $1s\sigma_g$ potential curve that contains a small dissociative portion (2 % of the total cross-section). Several dissociation channels can contribute to the formation of ions with higher momenta as summarized in Tables I and II, which report the kinetic energy of the ions H^+ and D^+ released in the molecular dissociation for different direct ionization channels ($1s\sigma_g$, $2p\sigma_u$ and $2p\pi_u$) and doubly excited states ($Q_1\,^1\Sigma_u^+(1)$, $Q_2\,^1\Sigma_u^+(1)$, $Q_2\,^1\Pi_u^+(1)$ and $Q_2\,^1\Pi_u^+(2)$) and for excitation photon energies comprised between 18.1 and 45 eV well matching the spectrum used in the experiment (inset of Fig. 1). The tables report the kinetic energy of the proton/deuteron E_k generated for different

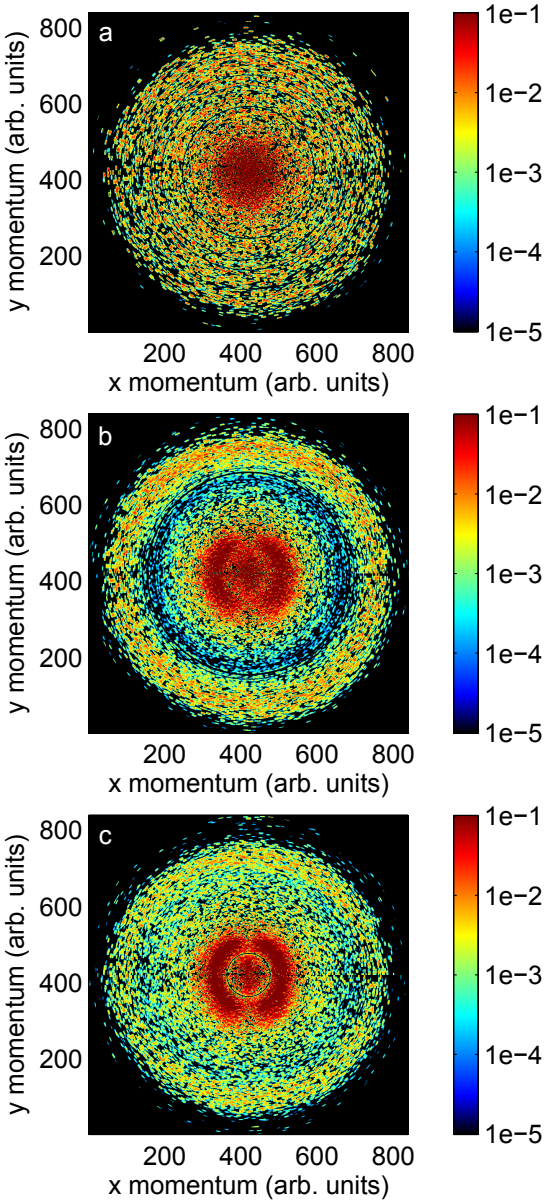

Fig. 2. 2D ion momentum distribution generated by the XUV pulse only (a), by the XUV and the few-cycle IR pulse for a delay $\tau = 0$ (b), and $\tau = 10$ fs (c). Both pulses were horizontally polarized

photon energy intervals (first row) and the ionization/excitation channel leading to the ion formation (first column). For the doubly excites states the autoionization channel is indicated. The information in Tables I and II was derived from ref. [15].

Doubly excited states Q_1 and Q_2 can either autoionize, producing a nuclear wave-packet on the $1s\sigma_g$ channel in the case of Q_1), on the $1s\sigma_g$ or $2p\sigma_u$ channels in the case of Q_2 or dissociate into neutral fragments (Q_1 and Q_2). It is important to observe that for photon energies below 30 eV the $Q_1\,^1\Sigma_u^+(1)$ is the dominant channel for the generation of high kinetic energy ions ($E_k > 1$ eV); in the energy range between 30 and 38 eV the direct ionization to the $2p\sigma_u$ and the autoionization channel $Q_2\,^1\Sigma_u^+(1) \rightarrow 2p\sigma_u$ dominate the generation of high kinetic energy ions via parallel transitions; on the other hand the autoionizing states $Q_2\,^1\Pi_u^+(1)$ and

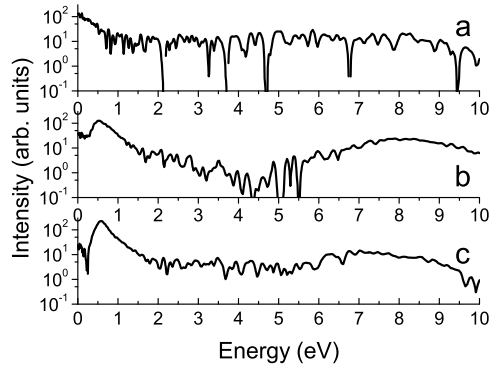

Fig. 3. Ion kinetic energy distribution generated by the XUV pulse only (a), by the XUV and the few-cycle IR pulse for a delay $\tau = 0$ (b), and $\tau = 10$ fs (c).

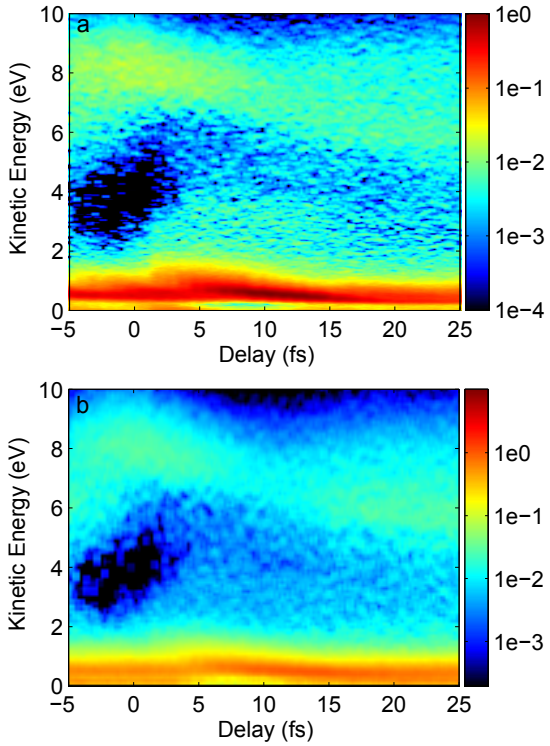

Fig. 4. Ion kinetic energy distribution as a function of the relative delay τ between the XUV and IR pulses, parallel (a) and perpendicular (b) to the laser polarization.

TABLE I
H^+ RELEVANT DISSOCIATION CHANNELS

	18.1-25 eV	25-30 eV	30-38 eV	38-45 eV
$1s\sigma_g$	$<$ 1eV	$<$ 1eV	$<$ 1eV	$<$ 1eV
$2p\sigma_u$	–	2-6 eV*	4-10 eV	5-10 eV
$2p\pi_u$	–	–	3-5 eV**	4-9 eV
$Q_1\ ^1\Sigma_u^+(1) \rightarrow 1s\sigma_g$	–	2-6 eV	x	x
$Q_2\ ^1\Sigma_u^+(1) \rightarrow 1s\sigma_g$	–	–	x	x
$Q_2\ ^1\Sigma_u^+(1) \rightarrow 2p\sigma_u$	–	–	4-10 eV	x
$Q_2\ ^1\Pi_u^+(1) \rightarrow 1s\sigma_g$	–	–	3-6.5 eV	x
$Q_2\ ^1\Pi_u^+(1) \rightarrow 2p\sigma_u$	–	–	6-9 eV	x
$Q_2\ ^1\Pi_u^+(2) \rightarrow 1s\sigma_g$	–	–	2-5.5 eV	x
$Q_2\ ^1\Pi_u^+(2) \rightarrow 2p\sigma_u$	–	–	4.5-7.5 eV	x

* energy threshold at 29.1 eV
** energy threshold at 35 eV
– energetically not allowed
x not identified or with vanishing contribution
First row: XUV photon energy range
First column: ionic/neutral states; in the case of doubly excited state, the decay channel is indicated

TABLE II
D^+ RELEVANT DISSOCIATION CHANNELS

	18.1-25 eV	25-30 eV	30-38 eV	38-45 eV
$1s\sigma_g$	$<$ 1eV	$<$ 1eV	$<$ 1eV	$<$ 1eV
$2p\sigma_u$	–	4-6 eV*	4-10 eV	5-10 eV
$2p\pi_u$	–	–	3-5 eV**	4-9 eV
$Q_1\ ^1\Sigma_u^+(1) \rightarrow 1s\sigma_g$	–	2-5 eV	2-5 eV	x
$Q_2\ ^1\Sigma_u^+(1) \rightarrow 1s\sigma_g$	–	–	x	x
$Q_2\ ^1\Sigma_u^+(1) \rightarrow 2p\sigma_u$	–	–	4-10 eV	x
$Q_2\ ^1\Pi_u^+(1) \rightarrow 1s\sigma_g$	–	–	3-6.5 eV	x
$Q_2\ ^1\Pi_u^+(1) \rightarrow 2p\sigma_u$	–	–	6-9 eV	x
$Q_2\ ^1\Pi_u^+(2) \rightarrow 1s\sigma_g$	–	–	2-5.5 eV	x
$Q_2\ ^1\Pi_u^+(2) \rightarrow 2p\sigma_u$	–	–	4.5-7.5 eV	x

* energy threshold at 29.8 eV
** energy threshold at 35 eV
– energetically not allowed
x not identified or with vanishing contribution
First row: XUV photon energy range
First column: ionic/neutral states; in the case of doubly excited state, the decay channel is indicated

$Q_2{}^1\Pi_u^+(2)$ strongly contribute to the generation of ions for perpendicular transitions. Finally for photon energies above 45 eV, the direct ionization channels $2p\sigma_u$ and $2p\pi_u$ dominate the generation of ions with $E_k > 1$ eV. Absolute cross sections for dissociative photoionization and the relative weight of the different channels can be found in [16], [17], [18].

The IR pulse strongly modifies the momentum distributions as shown in Fig. 2b and fig. 2c, corresponding to the time overlap ($\tau = 0$) and to an XUV-IR pulse delay of $\tau = 10$ fs (IR after the XUV), respectively. The distribution at $\tau = 0$ is characterized by an intense signal at low momenta and by an increase in the external part corresponding to high momenta; also a reduction in the intermediate region is visible (see Fig. 3b). The distribution acquired at $\tau = 10$ fs does not present such a pronounced reduction at intermediate momenta (see Fig. 3c). In order to distinguish the contribution of the different channels, the integration over the 3D momentum distribution parallel and perpendicular to the polarization axis (a cone with semi-aperture $\theta = 45^o$ was performed, and is reported in Fig. 4a and Fig. 4b, respectively. The IR pulse leads to a strong increase of the signal at low kinetic energies around $\tau \simeq 10$ fs [19]. The origin of this lies in the coupling between the $1s\sigma_g$ and $2p\sigma_u$ levels induced by the IR field and usually indicated as bond softening [20]. Single XUV photon ionization populates coherently several vibrational states of the $1s\sigma_g$ potential curve, producing an oscillating wave-packet in the binding potential. The IR pulse preferentially dissociates

the bound wave-packet when it reaches the outer turning point of the potential well after $\tau \simeq 10$ fs explaining the increase of the ion signal at low kinetic energies ($E_k < 1$ eV). The maximum of the ion yield in the bond softening channel was used as reference to determine the precise time overlap between the two pulses, knowing that the bound wave-packet in H_2^+ (D_2^+) requires 15 fs (22 fs) to reach the outer turning point of the $1s\sigma_g$ potential curve [21]. The strong enhancement of the signal in the region $8-10$ eV and the reduction in the region $3-6$ eV around the time overlap of the XUV and IR pulses is caused by an IR-induced mixing between the $2p\sigma_u$ and the $1s\sigma_g$ states. Also IR-ionization of doubly excited states $Q_1\ ^1\Sigma_u^+(1)$ could contribute to the enhancement at the highest energies. The ion distribution for the perpendicular direction shows an evolution similar to the parallel one. The bond softening mechanism is not so prominent as the coupling between the $1s\sigma_g$ and $2p\sigma_u$ is more effective for molecules aligned parallel to the IR laser polarization. The signal measured in the perpendicular direction indicates that a relevant contribution to the total momentum distribution comes from perpendicular transitions involving the doubly excited states $Q_2{}^1\Pi_u^+(1)$ and $Q_2{}^1\Pi_u^+(2)$. For photon energies above 42 ev, the perpendicular transition to the $2p\pi_u$ state can also contribute to the formation of high energy ions.

Using the angular distribution shown in Fig. 2, an asymmetry parameter for the ion emitted in the left and right directions, parallel to the laser polarization, was calculated according to the relation:

$$A(E_k,\tau) = \frac{N_L(E_k,\tau) - N_R(E_k,\tau)}{N_L(E_k,\tau) + N_R(E_k,\tau)} \tag{2}$$

where N_L and N_R are the number of ions emitted in the left and right direction, respectively. The asymmetry parameter indicates the degree of localization of the electron wave packet on the molecular ion; the experimental result is shown in Fig. 5 [22]. The asymmetry shows a complex dependence on the

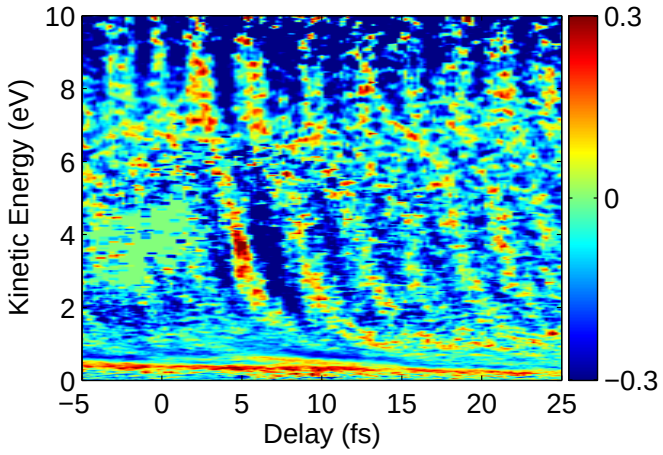

Fig. 5. Asymmetry according to Eq. 2 as a function of the relative delay τ between the XUV and IR pulses and the ion kinetic energy.

kinetic energy and on the relative delay and is characterized by a clear oscillation with the period of the IR field (T_0). The observation of an asymmetry in the ion yield implies, in general, the creation of coherent superposition of states with different parity; as previously discussed the attosecond pulse can excite/ionize the molecule/molecular ion to different levels that are accompanied by the ejection of an ion along either the $1s\sigma_g$ or the $2p\sigma_u$ channels. The electronic wave-functions ϕ_g and ϕ_u characterizing these levels may be viewed as the bonding and anti-bonding linear combination of $1s$ atomic wavefunctions on the left (L) and right (R) nucleus:

$$\phi_{g,u} = \frac{1}{\sqrt{2}}\left(\phi_{1s,L} \pm \phi_{1s,R}\right) \tag{3}$$

In order to localize the electron in the molecular ion a linear combinations of the eigenstates is required:

$$\phi_{L,R} = \frac{1}{\sqrt{2}}\left(\phi_g \pm \phi_u\right) \tag{4}$$

Experimentally the localization of the electron is observed as a laboratory asymmetry in the ejection of ionic fragments with respect to the laser polarization axis. In order for the electron localization to be observable, the coherent superposition must regard ions with the same final kinetic energies and with the same angular momentum of the outgoing electrons. The two electron wave function of the singly-ionized molecule can be written as:

$$\begin{aligned}\Phi(1,2) =& c_1[\phi_g(1)\chi(\varepsilon,l_g)(2)]_g + c_2[\phi_g(1)\chi(\varepsilon,l_u)(2)]_u + \\ &+ c_3[\phi_u(1)\chi(\varepsilon,l_u)(2)]_g + c_4[\phi_u(1)\chi(\varepsilon,l_g)(2)]_u\end{aligned} \tag{5}$$

with the electron 2 being described by a function of energy ε and angular momentum $l_{u,g}$. The observation of a localization of the remaining electron on the right or left nucleus in the laboratory frame, corresponds to the projection of $\Phi(1,2)$ on the localized states:

$$\Phi_{(L,R),(g,u)}(1,2) = \phi_{L,R}(1)\chi(\varepsilon,l_{g,u})(2) \tag{6}$$

The asymmetry can be therefore expressed as:

$$\begin{aligned}N_L - N_R = \sum_{i=g,u}\Big[&|<\Phi_{L,i}(1,2)\mid\Phi(1,2)>|^2 - \\ &|<\Phi_{R,i}(1,2)\mid\Phi(1,2)>|^2\Big] = 4\mathrm{Re}[c_1c_4^* + c_2c_3^*]\end{aligned} \tag{7}$$

Two main mechanisms responsible for the electron localization have been identified and will be discussed in the next two sections:

1) in analogy with single-color experiments IR [23] coupling between the $2p\sigma_u$ and the $1s\sigma_g$ during molecular dissociation can induce an electron localization and is observed for positive time delays (IR after XUV).

2) around the time overlap the presence of the IR field can affect the angular momentum state of the outgoing electron producing a coherent superposition state that is accompanied by an asymmetry in the laboratory frame. This mechanism involves the population of a dissociative wave-packet on the $1s\sigma_g$ through the autoionizing state Q_1. In order to correctly simulate this process a model based on the numerical integration of the 3-dimensional 2-electron time-dependent Schrödinger equation (TDSE) for H_2 molecules including electron correlation effects has to be considered. The results of this model will be presented in section V.

IV. SEMICLASSICAL INTERPRETATION

For the electron localization during the dissociation of H_2^+/D_2^+, only the interaction with the molecular ion is considered while the actual ionization is assumed to follow an idealized Franck-Condon projection of the neutral ground state. To date, many methods have been developed for modeling the interaction of H_2^+ with a strong laser field. Some of these methods make use of a grid representation of the electronic wavefunction in 3D or 1D configuration space, in combination with a wave packet description of the nuclear motion [24], [25]. Alternatively, the Born-Oppenheimer (BO) approximation can be invoked and one can propagate nuclear wave packets on a limited number of Born-Oppenheimer potential energy surfaces, where in practice the inclusion of the $1s\sigma_g$ and $2p\sigma_u$ states typically suffices [26]. This has the advantage that one can use known 3D potential energy curves, from which the effective potentials in reduced dimensional models show large deviations [25]. Use of the Born-Oppenheimer potential energy curves as the starting point for considering the interaction of H_2^+ with an intense laser field allows the development of insightful models that explain observations such as the occurrence of bond softening [20] and bond hardening [27]. These can be well understood by considering a description in terms of dressed states, where the laser coupling among the Born-Oppenheimer states is explicitly taken into account [28]. Here, we will consider the application of a semi-classical model that is based on a description in terms of quasi-static states that result from taking the laser-induced coupling among the Born-Oppenheimer states instantaneously (i.e. on a sub-cycle time scale) into account [29], [30]. It will be shown that the interaction that leads to localization of the electron can be understood in terms of a sequence of light-induced avoided crossings between the quasi-static states [22], [31]. The interaction of the dissociating molecular ion with the IR field couples the $1s\sigma_g$ and the $2p\sigma_u$ states and causes population to be transferred between the two states, resulting in a coherent superposition. The amplitudes in this superposition, and therefore the resulting degree of localization, depend on the precise shape of the electric field of the IR pulse within a finite window during the dissociation as will be shown later. The total wave-function can be written as:

$$\Psi(R,t) = \psi_g(R,t)\phi_g(R) + \psi_u(R,t)\phi_u(R) \tag{8}$$

with R the internuclear distance and t the time. The electronic wavefunctions $\phi_{g,u}$ (see (3)) depend parametrically on R. $\psi_g(R,t)$ and $\psi_u(R,t)$ are functions describing the nuclear wave-packet on the two laser-coupled Born-Oppenheimer potential curves associated with the $1s\sigma_g$ and the $2p\sigma_u$ of H_2^+/D_2^+, respectively.

The TDSE is solved numerically with the hamiltonian expressed in the basis of the field free eigenstates:

$$H_{total}(R,t) = T(R) + H_{int}(R,t) \tag{9}$$

with

$$T(R) = \begin{pmatrix} -\frac{1}{2m_{red}}\frac{\partial^2}{\partial R^2} & 0 \\ 0 & -\frac{1}{2m_{red}}\frac{\partial^2}{\partial R^2} \end{pmatrix}$$
$$H_{int}(R,t) = \begin{pmatrix} V_g(R) & V_{laser}(R,t) \\ V_{laser}(R,t) & V_u(R) \end{pmatrix} \tag{10}$$

with $V_g(R)$ and $V_u(R)$ the potential energies, V_{laser} the dipole coupling term defined by $V_{laser} = -\mu(R)E(t)$ with $\mu(R)$ the dipole moment and $E(t)$ the electric field of the IR pulse and m_{red} the reduced mass. In relation to Eq. 3 and Eq. 4 we can define localized nuclear wave-functions ψ_L and ψ_R given by:

$$\psi_{L,R} = \frac{1}{\sqrt{2}}\left(\psi_g \pm \psi_u\right) \tag{11}$$

and representing states associated to the localized electron wave functions $\phi_{L,R}$. Figure 6 shows the populations in the field-free states ψ_g and ψ_u (Fig. 6b) and the localized states (Fig. 6e) of Eq. 11 integrated over all fragment kinetic energies, for the laser field shown in Fig. 6a. Referring back to Eq. 5, the IR-induced coupling creates a localization by creating a superposition states that are accompanied by the same angular momentum of the outgoing electron (i.e c_2 in combination with c_3, resp. c_1 in combination with c_4). It is immediately clear from Fig. 6 that there is not intuitive interpretation for the dynamics expressed in the field-free states, nor is the translation from populations associated with ψ_g and ψ_u to the localized populations associated with ψ_L and ψ_R straightforward. Introduction of the quasi-static states will allow us to develop an interpretation of the dynamics.

The quasi-static states are the eigenstates of the interaction hamiltonian in Eq. 10 for a given value of the electric field $E(t)$ [29], [30]. Diagonalization of the hamiltonian leads to the following expression for the quasi-static states:

$$\psi_1(R,t) = \cos\theta(R,t)\psi_g(R) + \sin\theta(R,t)\psi_u(R)$$
$$\psi_2(R,t) = -\sin\theta(R,t)\psi_g(R) + \cos\theta(R,t)\psi_u(R) \tag{12}$$

where the time-dependent mixing parameter $\theta(R,t)$ is given by [30]:

$$\tan\left(2\theta(R,t)\right) = -\frac{2V_{laser}(R,t)}{\omega_0(R)} \tag{13}$$

The resulting quasi-static eigenvalues $V_{1,2}(R,t)$ are:

$$V_{1,2}(R,t) = \frac{V_g(R)+V_u(R)}{2} \mp \sqrt{\frac{\omega_0(R)^2}{4} + V_{laser}(R,t)^2} \tag{14}$$

with $\omega_0(R) = V_u(R) -)V_g(R)$ the energy spacing between the two levels. From this description it can be seen that the nature of the quasi-static states depends on the internuclear distance and time: for $V_{laser}(R,t) \ll \omega_0(R)$, in the early stages of the dissociation the coupling is weak, i.e. $\theta \approx 0$, $\psi_1 \approx \psi_g$ and $\psi_2 \approx \psi_u$. Towards the end of the dissociation, for $V_{laser}(R,t) \gg \omega_0(R)$, when - for all but a vanishing laser intensity - the separation between the Born-Oppenheimer potential energy curves becomes negligible compared to the laser coupling, we have $\theta \approx \frac{\pi}{4}$, $\psi_1 \approx \psi_L$ and $\psi_2 \approx -\psi_R$ if $V_{laser}(R,t) < 0$, and $\psi_1 \approx \psi_R$ and $\psi_2 \approx \psi_L$ if $V_{laser}(R,t) > 0$ $\theta \approx -\frac{\pi}{4}$. In this limit the quasi-static states

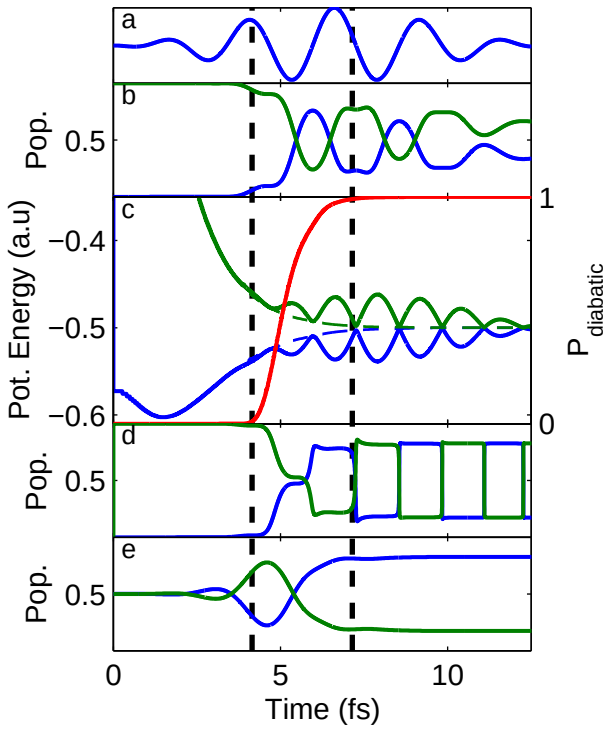

Fig. 6. (a) 4.8 fs FWHM 800 nm laser pulse; (b) population dynamics during dissociation shown in the field-free states $1s\sigma_g$ (blue) and $2p\sigma_u$ (green); (c) time-dependent potential energies of the quasi-static states during molecular dissociation of D_2 in the presence of the laser field depicted in (a) with a peak intensity of 3.5×10^{12} W/cm^2. The red curve shows the probability for a non-adiabatic transition given by the Landau-Zener formula, and defines the three regions, delimited by the vertical dashed lines, where the dynamics is primarily adiabatic (left region), primarily diabatic (right region) or mixed (central region). (d-e) population dynamics during dissociation shown in (d) the quasi-static states '1' (green) and '2' (blue) and (e) the localized states 'left' (green) and 'right' (blue).

describe localized electronic states where the electron resides on the left, resp. right proton. To describe the dynamics in terms of the quasi-static states the following wavefunction is used:

$$\Psi(R,t) = \psi_1(R,t)\phi_1(R,t) + \psi_2(R,t)\phi_2(R,t) \tag{15}$$

with $\phi_{1,2}$ the time-dependent quasi-static states. Inserting this into the time-dependent Schrödinger equation using the diagonalized hamiltonian and realizing that from the definition of the quasi-static states it follows that:

$$\begin{aligned} \dot{\phi_1} &= +\dot{\theta}\phi_2 \\ \dot{\phi_2} &= -\dot{\theta}\phi_1 \end{aligned} \tag{16}$$

leads to

$$i\begin{pmatrix}\dot{\psi}_1(R,t)\\ \dot{\psi}_2(R,t)\end{pmatrix} = \begin{pmatrix} V_1(R,t) & i\dot{\theta}(R,t) \\ -i\dot{\theta}(R,t) & V_2(R,t)\end{pmatrix}\begin{pmatrix}\psi_1(R,t)\\ \psi_2(R,t)\end{pmatrix} \tag{17}$$

which shows that $\dot{\theta}(R,t)$ acts as an effective coupling term between the two quasi-static states. $\dot{\theta}(R,t)$ can be derived from Eq. 13:

$$\dot{\theta}(R,t) = -\frac{\dot{V}_{g,u}(R,t)\omega_0(R)}{\omega_0(R)^2 + 4V_{laser}(R,t)^2} \tag{18}$$

$\dot{\theta}(R,t)$, and thus the population transfer, peaks around the zero crossings of the laser field $E(t) = 0$ when avoided crossings occur between the quasi-static states. The magnitude of the population transfer depends on the relative size of $\dot{\theta}(R,t)$ with respect to the difference $V_2 - V_1$. At a zero crossing of the laser field it follows from Eq. 18: $\dot{\theta}(R,t) = \mu(R)E_0(t)\ \omega_l/\omega_0(R)$ where ω_l is the laser frequency and $E_0(t)$ is the envelope of the laser field. The wave packet dynamics can be split up into three regions. In the beginning, when $\omega_0^2 \gg \mu E_0 \omega_l$, the dynamics is adiabatic, i.e. populations remain in the initial quasi-static state. At the end of the dissociation when $\omega_0^2 \ll \mu E_0 \omega_l$, the dynamics becomes completely diabatic and at a zero-crossing of the field the dissociating wave packet hops from one quasi-static state to the other, leaving any existing electron localization intact. The electron localization is established in an intermediate region where the dynamics is neither adiabatic nor diabatic. In this regime, the wave packet traverses one or more avoided crossings where the degree of adiabaticity determines the extent of the localization that will asymptotically be measured. This can be illustrated for the situation considered in Fig. 6 by plotting the quasi-static potentials as a function of time (Fig. 6c) revealing the laser-induced avoided crossings. In Fig. 6d, where the populations $|\psi_1(R,t)^2|$ and $|\psi_2(R,t)^2|$ are shown, the transitions between the two states are concentrated around the avoided crossings. Moreover, the three regions of adiabaticity of the transitions can be clearly distinguished and are marked by the dashed lines in Fig. 6.

This interpretation of the molecule-laser interaction in terms of transitions between quasi-static states at a finite number of avoided crossings can form the basis of a semi-classical model. In such a model the passages through these avoided crossings can be described by a Landau-Zener formula. Nuclear trajectories are calculated on the basis of a weighted average of the two quasi-static potential energy curves, with relative weights according to the instantaneous populations. In determining the trajectories the effect of the electric field on the nuclear dynamics is taken into account [30]. Trajectories are started from all nuclear distances within the Franck-Condon (FC) region and the starting position of a trajectory within the FC region determines the final kinetic energy of the nuclei. For each trajectory an instantaneous population exchange is made at the zero crossings of the laser field. The size of the transfer is calculated by a Landau-Zener formula [29], [32]:

$$P_{diabatic}(R,t) = \ e^{-\frac{\pi\omega_0(R)^2}{4\omega_l\mu(R)E_0(t)}} \tag{19}$$

Since more than one crossing is relevant to the dynamics, the phase difference $\Delta\phi$ that develops between the amplitudes in the upper and lower quasi-static state between two avoided crossings has to be taken into account. It is given by:

$$\Delta\phi = -i\int_{t_0}^{t_0+\frac{T}{2}} \left(V_1(t') - V_2(t')\right) dt' \tag{20}$$

The sign of the amplitude transfer at an avoided crossing is determined from the sign of $\dot{\theta}(R,t)$ in Eq. 18 which is directly related to the sign of the derivative of the electric field $\dot{E}(t)$:

$$\text{sgn}\ (\dot{\theta}) = -\text{sgn}\ \dot{V}_{g,u} = \text{sgn}\ \dot{E(t)} \tag{21}$$

In Fig. 7 the asymmetry parameter as a function of kinetic energy and delay determined with this semi-classical method (Fig. 7b) is compared to a Time-Dependent Schrödinger Equation (TDSE) calculation (Fig. 7a). These calculations are performed for D_2^+ and a 4.8 fs FWHM IR field with a central wavelength of 800 nm. The two calculations show a behavior that is very similar to the experimental observation and moreover show satisfactory agreement, validating the interpretation of the TDSE results in terms of non-adiabatic transitions between the quasi-static states. The observed energy correlation between the fragment kinetic energy and the time delay is due to the fact that the internuclear distance where a trajectory starts governs both the asymptotic kinetic energy and the internuclear distance where the curve-crossings take place, impacting on the Landau-Zener transition probability. The intensity dependence of the asymmetry calculated with

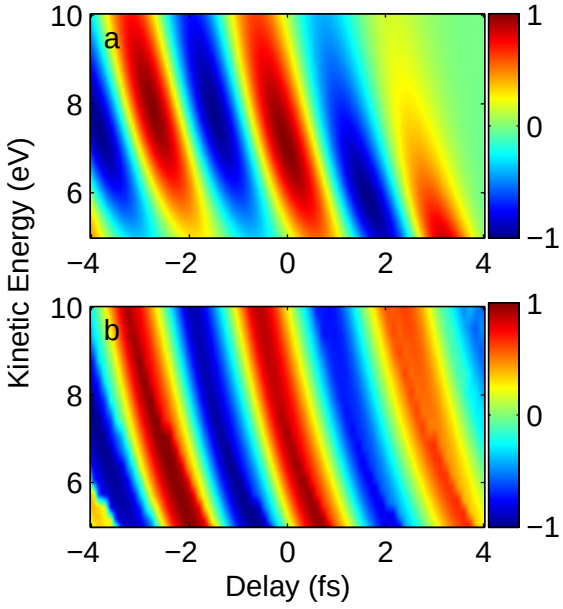

Fig. 7. Asymmetry parameter $A(E_k, \tau)$ of D^+ fragments as a function of the delay τ between an isolated attosecond pulse that promotes a Frank-Condon wave packet onto the $2p\sigma_u$ state and the center of a 4.8 fs FWHM, 800 nm pulse with a peak intensity of 3.5×10^{12} W/cm^2, and fragment kinetic energy E_k, (a) in the 1D TDSE model and (b) in the semi-classical model.

the semi-classical method is shown in Fig. 8 for a trajectory that starts in the center of the Franck Condon region. The result is compared to the result of a TDSE calculation of the asymmetry at the maximum of the fragment yield [33]. The general trend of the intensity dependence in the TDSE model is well-reproduced by the semi-classical model.

V. Ab-initio model: role of electron correlation

A. Formalism

The 3D 2-electron model implemented to describe the localization process is based on solution of the TDSE within the dipole approximation:

$$[\mathcal{H}_{el}(\mathbf{r}_1, \mathbf{r}_2, R) + T(R) + (\mathbf{p}_1 + \mathbf{p}_2) \cdot \mathbf{A}(t) - i\partial_t] \Phi(\mathbf{r}_1, \mathbf{r}_2, R, t) = 0 \quad (22)$$

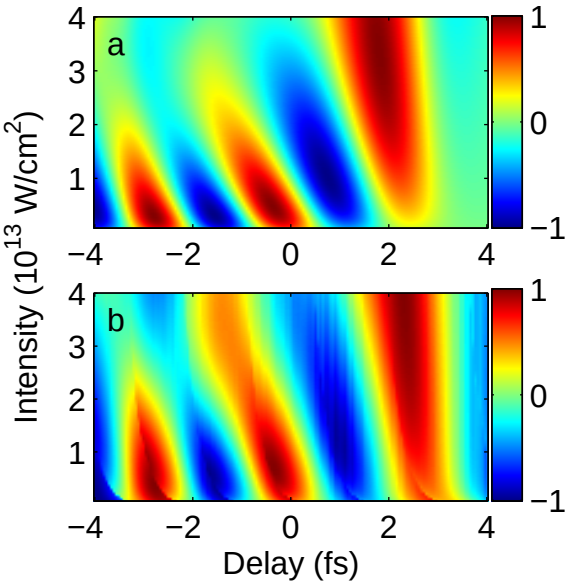

Fig. 8. Asymmetry parameter at fragment kinetic energy corresponding to center of the nuclear wave packet as a function of delay and intensity for the TDSE (a) and the semi-classical (b) model.

where $\mathcal{H}_{el}$ is the electronic Hamiltonian, $T(R)$ the kinetic energy operator of the nuclei and $\mathbf{A}(t)$ is the vector potential of the laser field.

The time dependent wave function $\Phi(\mathbf{r}_1, \mathbf{r}_2, R, t)$ is expanded in a basis of fully correlated adiabatic Born-Oppenheimer (BO) vibronic stationary states of energy W_k, which includes the bound states, the doubly excited states and the non-resonant continuum states of H_2:

$$\Phi(\mathbf{r}_1, \mathbf{r}_2, R, t) = \sum_b C_{b\nu_b}(t)\phi_b(\mathbf{r}_1, \mathbf{r}_2, R)\chi_{\nu_b}(R)e^{-iW_{\nu_g}t} + \sum_r \sum_{\nu_r} C_{r\nu_r}(t)\phi_r(\mathbf{r}_1, \mathbf{r}_2, R)\chi_{\nu_r}(R)e^{-iW_{\nu_r}t} + \sum_{\alpha\ell} \int d\varepsilon \sum_{\nu_\alpha} C^{\varepsilon\ell m}_{\alpha\nu_\alpha}(t)\psi^{\varepsilon\ell}_\alpha(\mathbf{r}_1, \mathbf{r}_2, R)\chi_{\nu_\alpha}(R)e^{-iW_{\nu_\alpha}t} \quad (23)$$

where ϕ_b, ϕ_r and $\psi^{\varepsilon\ell}_\alpha$ represent the bound, doubly excited and continuum electronic states of H_2, respectively. These electronic states result from the solution of the following eigenvalue equations:

$$[\mathcal{H}_{el} - E_b(R)]\,\phi_b = 0 \quad (24)$$

$$[\mathcal{Q}\mathcal{H}_{el}\mathcal{Q} - E_r(R)]\,\phi_r = 0 \quad (25)$$

$$[\mathcal{P}\mathcal{H}_{el}\mathcal{P} - E^\varepsilon_\alpha(R)]\,\psi^{\varepsilon\ell}_\alpha = 0 \quad (26)$$

where $\mathcal{P}$ and $\mathcal{Q} = 1 - \mathcal{P}$ are Feshbach projection operators that project onto the resonant and non-resonant parts of the continuum wave function. Here, α denotes the full set of quantum numbers for the electronic state of the residual molecular ion H_2^+ with BO energy $E_\alpha(R)$ and the indices ℓ and ε correspond, respectively, to the angular momentum and kinetic energy of the ejected electron. More details can

be found in ref. [34]. The vibrational (bound and dissociative) wave functions χ_{ν_b}, χ_{ν_r} and χ_{ν_α} are the solutions of a one-dimensional Schrödinger equation that represents the relative motion of the two nuclei in the presence of the potentials $E_b(R)$, $E_r(R)$ and $E^{\varepsilon}_{\alpha}(R)$, respectively.

B. Description of the observables

To evaluate the different observables, the time dependent wave function given in eq. (23) must be projected onto different asymptotic states. In dissociative ionization experiments in which the electron and proton momenta are fully determined, one must project onto singlet states of the following form:

$$\begin{aligned} |R\rangle &= \frac{1}{\sqrt{2}}\sum_{\ell m} i^{\ell} e^{-i\sigma_\ell(\varepsilon)} \mathcal{Y}^{m*}_{\ell}(\mathbf{k})[\psi^{\varepsilon\ell}_{g}(\mathbf{r}_1,\mathbf{r}_2;R)\chi_{\nu_g}(R) \\ &\quad \times e^{-iW_g t} + \psi^{\varepsilon\ell}_{u}(\mathbf{r}_1,\mathbf{r}_2;R)\chi_{\nu_u}(R)e^{-iW_u t}] \\ |L\rangle &= \frac{1}{\sqrt{2}}\sum_{\ell m} i^{\ell} e^{-i\sigma_\ell(\varepsilon)} \mathcal{Y}^{m*}_{\ell}(\mathbf{k})[\psi^{\varepsilon\ell}_{g}(\mathbf{r}_1,\mathbf{r}_2;R)\chi_{\nu_g}(R) \\ &\quad \times e^{-iW_g t} - \psi^{\varepsilon\ell}_{u}(\mathbf{r}_1,\mathbf{r}_2;R)\chi_{\nu_u}(R)e^{-iW_u t}] \end{aligned} \quad (27)$$

where R stands for protons ejected to the right (H + H^+) and L for protons ejected to the left (H^+ + H), g and u stands for $1s\sigma_g$ and $2p\sigma_u$ respectively, $\sigma_\ell(\varepsilon) = \mathrm{arg}\Gamma\left(\ell+1-i/\sqrt{2\varepsilon}\right)$ is the Coulomb phase shift and $\mathcal{Y}_{\ell m}$ is a spherical harmonic. The corresponding differential (in electron energy, electron emission direction, proton energy, and proton emission hemisphere) dissociative ionization probability is given by

$$\frac{d^3P^{\Gamma}}{dE_{H^+}d\varepsilon d\Omega} = \frac{1}{2}\left|\sum_{\alpha\ell m} i^{-\ell}e^{i\sigma_\ell(\varepsilon)}\mathcal{Y}^{m}_{\ell}(\Omega)C^{\varepsilon\ell}_{\alpha\nu}\right|^2 \quad (28)$$

where Γ stands for R or L[1].

Notice that, in writing eq. (27), we have taken into account that, below ∼35 eV, the R and L paths mainly result from the combination of the $1s\sigma_g$ and $2p\sigma_u$ H_2^+ molecular states into 1s orbitals localized in just one of the protons(see Eq. 4).

When the experiment does not determine the electron energy, the dissociative ionization probability is obtained by integrating Eq. (28) over the electron kinetic energy:

$$\frac{d^2P^{\Gamma}}{dE_{H^+}d\Omega} = \frac{1}{2}\int d\varepsilon \left|\sum_{\alpha\ell m} i^{-\ell}e^{i\sigma_\ell(\varepsilon)}\mathcal{Y}^{m}_{\ell}(\Omega)C^{\varepsilon\ell}_{\alpha\nu}\right|^2 \quad (29)$$

When the electron emission direction is not determined either, one must integrate the latter equation over the electron solid angle:

$$\frac{dP^{\Gamma}}{dE_{H^+}} = \frac{1}{2}\int d\varepsilon \sum_{\ell}\sum_{\alpha\alpha'} C^{\varepsilon\ell *}_{\alpha'\nu_{\alpha'}} C^{\varepsilon\ell}_{\alpha\nu_\alpha} \quad (30)$$

In order to compare with experiments, we have also evaluated the proton asymmetry parameter defined as:

$$\beta(E_{H^+}) = \frac{\left(\frac{dP^L}{dE_{H^+}} - \frac{dP^R}{dE_{H^+}}\right)}{\left(\frac{dP^L}{dE_{H^+}} + \frac{dP^R}{dE_{H^+}}\right)} \quad (31)$$

[1]We set the R direction by $C^{\varepsilon\ell}_{(\alpha=u)\nu_\alpha} \rightarrow C^{\varepsilon\ell}_{u\nu_\alpha}$ and the L by $C^{\varepsilon\ell}_{(\alpha=u)\nu_\alpha} \rightarrow -C^{\varepsilon\ell}_{u\nu_u}$.

where

$$\frac{dP^R}{dE_{H^+}} = \frac{1}{2}\int d\varepsilon \sum_{\ell}\left(|C^{\varepsilon\ell}_{g\nu_g}|^2 + 2\mathrm{Re}[C^{\varepsilon\ell *}_{g\nu_g}C^{\varepsilon\ell}_{u\nu_u}] + |C^{\varepsilon\ell}_{u\nu_u}|^2\right), \quad (32)$$

$$\frac{dP^L}{dE_{H^+}} = \frac{1}{2}\int d\varepsilon \sum_{\ell}\left(|C^{\varepsilon\ell}_{g\nu_g}|^2 - 2\mathrm{Re}[C^{\varepsilon\ell *}_{g\nu_g}C^{\varepsilon\ell}_{u\nu_u}] + |C^{\varepsilon\ell}_{u\nu_u}|^2\right) \quad (33)$$

and

$$\begin{aligned} \frac{dP}{dE_{H^+}} &= \frac{dP^R}{dE_{H^+}} + \frac{dP^L}{dE_{H^+}} \\ &= \int d\varepsilon \sum_{\ell}\left(|C^{\varepsilon\ell}_{g\nu_g}|^2 + |C^{\varepsilon\ell}_{u\nu_u}|^2\right). \end{aligned} \quad (34)$$

Substituting the latter equations in the definition of the proton asymmetry parameter we obtain

$$\beta(E_{H^+}) = 2\int d\varepsilon \sum_{\ell}\left(\mathrm{Re}[C^{\varepsilon\ell *}_{g\nu_g}C^{\varepsilon\ell}_{u\nu_u}]\right)/\frac{dP}{dE_{H^+}} \quad (35)$$

Notice that the asymmetry arises from the interference between the $1s\sigma_g$ and $2p\sigma_u$ channels in the numerator.

As explained above, equation (29) gives the Molecular Frame Photoelectron Angular Distributions (MFPADs) for a H+H^+ or H^++H process. We may also define an electron asymmetry parameter as:

$$\alpha^{\Gamma}(E_{H^+}) = \frac{\left(\frac{dP^{\Gamma l}}{dE_{H^+}} - \frac{dP^{\Gamma r}}{dE_{H^+}}\right)}{\left(\frac{dP^{\Gamma l}}{dE_{H^+}} + \frac{dP^{\Gamma r}}{dE_{H^+}}\right)} \quad (36)$$

where

$$\frac{dP^{\Gamma_r}}{dE_{H^+}} = \int_0^{\frac{\pi}{2}} \sin\theta d\theta \int_0^{2\pi} d\phi \frac{d^2P^{\Gamma}}{dE_{H^+}d\Omega} \quad (37)$$

$$\frac{dP^{\Gamma_l}}{dE_{H^+}} = \int_{\frac{\pi}{2}}^{\pi} \sin\theta d\theta \int_0^{2\pi} d\phi \frac{d^2P^{\Gamma}}{dE_{H^+}d\Omega} \quad (38)$$

Equation (36) defines the asymmetry related to the electron angular distributions for protons escaping to the left α^L or to the right α^R. Of course, this asymmetry depends on the proton kinetic energy and also on the time delay between the pump and probe pulses, i.e. $\alpha^{\Gamma} = \alpha^{\Gamma}(E_{H^+},\tau)$.

C. Results

Figure 9 shows the dissociative ionization probability as a function of the time delay between the pump and probe pulses and also as a function of the proton kinetic energy (left panel) and the electron kinetic energy (right panel). Figure 9 reproduces several features experimentally observed (Fig. 4), such as the increase of the bond softening channel for time delays around $\tau = 10$ fs and the increase of the signal for high kinetic energy protons at the time overlap. The 3D 2-electron model also predicts oscillations in the dissociation probability that were not observed in the experiment, due to the poor signal to noise ratio; evidences for such oscillations using different experimental conditions were recently obtained.

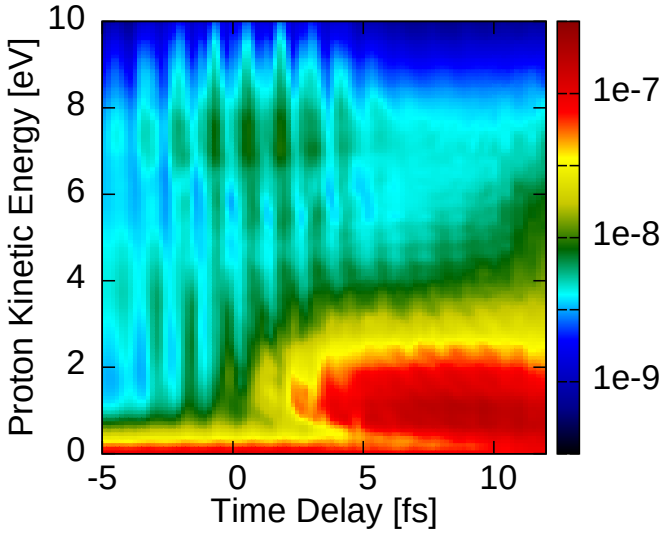

Fig. 9. Dissociative ionization probability as a function of the proton kinetic energy and time delay between the pulses. XUV pulse parameters: time duration 145 as (FWHM), intensity 1×10^9 W/cm^2 and central photon energy 30 eV. IR pulse parameters: time duration 5.8 fs (FWHM), intensity 3×10^{12} W/cm^2 and central photon energy 1.65 eV

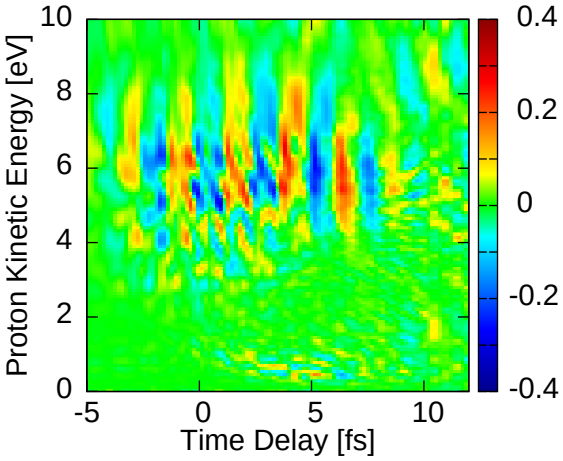

Fig. 10. Asymmetry parameter for the formation of H^+ in the left/right direction as a function of the proton kinetic energy and the time delay between the pulses.

Figure 10 shows the proton asymmetry parameter as a function of the time delay between the pump and the probe pulse and of the proton kinetic energy. The oscillations in the asymmetry observed in the experiments are reproduced in the model. In particular the model shows an asymmetry for kinetic energy $E_k > 4$ eV and at the time overlap between the two pulses. The origin of the asymmetry is due to two paths involving direction ionization to the $2p\sigma_u$ level and excitation of the Q_1 states that autoionize populating the $1s\sigma_g$ state, emitting an electron mostly characterized by a p-wave (in Eq. 5 this corresponds to $c_2 \neq 0$). Without IR field the direct ionization to the $2p\sigma_u$ level is linked to the emission of an electron in an s-wave. Considering Eq. 5 such a channel corresponds to $c_4 \neq 0$. The IR redistributes the outgoing electron wave-packet among different angular momentum states ($c_3 \neq 0$), creating a coherent superposition of $1s\sigma_g$ and $2p\sigma_u$ for the same proton kinetic energy and for the same angular momentum of the outgoing electron. The mechanism responsible for the asymmetry during the molecular dissociation is only weakly visible in Fig. 10, mainly due to the restriction in IR intensity $I < 3 \times 10^{12} W/cm^{-2}$ and due to the excitation in the calculation only of states with Σ symmetry. However such a mechanism is relevant in the experiment and can be reproduced using the semi-classical model reported in section IV. The oscillations in the asymmetry parameter clearly visible in Fig. 5 at low kinetic energies are not reproduced in the simulated asymmetry parameter shown in Fig. 10, probably due to the different timescales for photodissociation between the experiment (performed in D_2) and the simulation (performed in H_2). Comparison between Fig. **??** and experimental data acquired in H_2 (shown in Fig. 2c of [22]) shows a better agreement of the evolution of the asymmetry parameter also in the low kinetic energy region.

VI. Conclusion

Using isolated attosecond pulses and CEP-stable IR laser fields, the electron localization of a H_2/D_2 molecule undergoing dissociation can be finely controlled. The mechanism underlying this control is the IR-induced coupling of states of different symmetry that are populated directly through photo-ionization or indirectly by autoionization of doubly excited states. The presence of 2-electron processes, requires the application of a 3D ab-initio model taking into account electron correlation to properly describe the population of the $1s\sigma_g$ and $2p\sigma_u$ states. Simplified models based on the solution of a 1D-TDSE allow to gain physical insight in the localization mechanism during molecular dissociation. These results represent the starting point for the investigation of new schemes for the control of electronic density distributions during chemical processes applying attosecond pulses.

Acknowledgment

Financial support by the Alexander von Humboldt Foundation (Project "Tirinto"), the Ateneo italo-tedesco (Programma-Vigoni 2007-2009), the Italian Ministry of Research (Project FIRB No. RBID08CRXK), and the Marie Curie Research Training Networks XTRA is gratefully acknowledged. This work is part of the research program of the "Stichting voor Fundamenteel Onderzoek der Materie (FOM)", which is financially supported by the "Nederlandse Organisatie voor Wetenschappelijk Onderzoek (NWO)". We thank Mare Nostrum BSC and CCC-UAM for allocation of computer time. Work partially supported by the MICINN project Nos. FIS2010-15127, ACI2008-0777 and CSD 2007-00010, and the European COST Action CM0702.

REFERENCES

[1] A. Rudenko, Th. Ergler,, B. Feuerstein, K. Zrost, C. D. Schröter, R. Moshammer and J. Ullrich, *Chem. Phys.* **329**, 193 (2006).
[2] D. Polli, P. Alto, O. Weingart, K. M. Spillane, C. Manzoni, D. Brida, G. Tomasello, G. Orlandi, P. Kukura, R. A. Mathies, M. Garavelli and G. Cerullo, *Nature* **467** (2010).
[3] R. Neutze, R. Wouts, D. van der Spoel, E. Weckert and J. Hajdu, *Nature* **406**, 752 (2000).
[4] H. J. Wörner, J. B. Bertrand, D. V. Kartashov, P. B. Corkum and D. M. Villeneuve, *Nature* **466**, 604 (2010).
[5] P. M. Paul, E. S. Toma, P. Breger, G. Mullot, F. Augé, Ph. Balcou, H. G. Muller and P. Agostini, *Science* **292**, 1689 (2001).
[6] M. Hentschel, R. Kienberger, Ch. Spielmann, G. A. Reider, N. Milosevic, T. Brabec, P. Corkum, U. Heinzmann, M. Drescher and F. Krausz, *Nature* **414**, 509 (2001).
[7] F. Remacle and R. D. Levine, *PNAS* **103**, 6793 (2006).
[8] D. R. Yarkony, *Rev. Mod. Phys.* **68**, 985 (1996).
[9] J. L.Sanz-Vicario, H. Bachau and F. Martín, *Phys. Rev. A* **73**, 033410 (2006).
[10] T. Jahnke, A. Czasch, M. S. Schöffler, S. Schössler, A. Knapp, M. Käsz, J. Titze, C. Wimmer, K. Kreidi, R. E. Grisenti, A. Staudte, O. Jagutzki, U. Hergenhahn, H. Schmidt-Böcking, and R. Dörner, *Phys. Rev. Lett.* **93**, 163401 (2004).
[11] L. S. Cederbaum, *J. Chem. Phys.* **128**, 124101 (2008).
[12] G. Sansone, E. Benedetti, F. Calegari, C. Vozzi, L. Avaldi, R. Flammini, L. Poletto, P. Villoresi, C. Altucci, R. Velotta, S. Stagira, S. De Silvestri and M. Nisoli, *Science* **314**, 443 (2006).
[13] K. S. Budil, P. Saliéres, M. D. Perry and A. LHuillier, *Phys. Rev. A* **48**, R3437 (1993).
[14] I. J. Sola, E. Mével, L. Elouga, E. Constant, V. Strelkov, L. Poletto, P. Villoresi, E. Benedetti, J. P. Caumes, S. Stagira, C. Vozzi, G. Sansone and M. Nisoli, *Nature Physics* **2**, 319 (2006).
[15] K. Ito, R. I. Hall and M. Ukai, *J. Chem. Phys.* **104**, 8449 (1996).
[16] Y. M. Chung, E.-M. Lee, T. Masuoka and J. A. R. Samson, *J. Chem. Phys.* **99**, 885 (1993).
[17] I. Sánchez and F. Martín, *Phys. Rev. A* **57**, 1006 (1998).
[18] I. Sánchez and F. Martín, *Phys. Rev. A* **60**, 2200 (1999).
[19] F. Kelkensberg, C. Lefebvre, W. Siu, O. Ghafur, T. T. Nguyen-Dang, O. Atabek, A. Keller, V. Serov, P. Johnsson, M. Swoboda, T. Remetter, A. LHuillier, S. Zherebtsov, G. Sansone, E. Benedetti, F. Ferrari, M. Nisoli, F. Lépine, M. F. Kling and M. J. J. Vrakking, *Phys. Rev. Lett.* **103**, 123005 (2009)
[20] P. H. Bucksbaum, A. Zavriyev, H. G. Muller and D. W. Schumacher, *Phys. Rev. Lett.* **64**, 1883 (1990).
[21] C. D. Lin, X. M. Tong and T. Morishita, *J. Phys. B: At. Mol. Opt. Phys.* **39**, S419 (2006).
[22] G. Sansone, F. Kelkensberg, J. F. Pérez-Torres, F. Morales, M. F. Kling, W. Siu, O. Ghafur, P. Johnsson, M. Swoboda, E. Benedetti, F. Ferrari, F. Lépine, J. L. Sanz-Vicario, S. Zherebtsov, I. Znakovskaya, A. L'Huillier, M. Y. Ivanov, M. Nisoli, F. Martín and M. J. J. Vrakking, *Nature* **465**, 763 (2010).
[23] M. F. Kling, Ch. Siedschlag, A. J. Verhoef, J. I. Khan, M. Schultze, Th. Uphues, Y. Ni, M. Uiberacker, M. Drescher, F. Krausz and M. J. J. Vrakking, *Science* **312**, 246 (2006).
[24] S. Chelkowski, T. Zuo, O. Atabek and A. D. Bandrauk, *Phys. Rev. A* **52**, 2977 (1995).
[25] K. C. Kulander, F. H. Mies and K. J. Schafer, *Phys. Rev. A* **53**, 2562 (1996).
[26] A. D. Bandrauk, *Molecules in Laser Field* M. Dekker, New York, 1994.
[27] A. Giusti-Suzor and F. H. Mies, *Phys. Rev. Lett.* **68**, 3869 (1992).
[28] A. Bandrauk and M. L. Sink, *J. Chem. Phys.* **74**, 1110 (1981).
[29] P. Dietrich, M. Yu. Ivanov, F. A. Ilkov and P. B. Corkum, *Phys. Rev. Lett.* **77**, 4150 (1996).
[30] I. Kawata, H. Kono and Y. Fujimura, *J. Chem. Phys.* **110**, 11152 (1999).
[31] F. Kelkensberg, G. Sansone, M. Yu. Ivanov and M. J. J. Vrakking, *submitted*.
[32] M. Tachuk, M. Yu Ivanov and D. M. Wardlaw, *J. Chem. Phys.* **109**, 5747 (1998).
[33] F. He, A. Becker and U. Thumm, *Phys. Rev. Lett* **101**, 213002 (2008).
[34] J. L. Sanz-Vicario, H. Bachau and F. Martín, *Phys. Rev. A* 73, 033410 (2006).

PLACE PHOTO HERE

I n 2004 he received the Ph.D. degree in Physics from the Politecnico of Milan with an experimental thesis on the effects of the CEP on the HHG process. In 2007 he was at the Laser Technology Laboratory at RIKEN, Wako Saitama in Japan as Short term Post-Doc of the JSPS foundation. In 2008 he was at the Department of Chemistry of the Tokyo University as visiting scientist. In 2009-2010 he joined the Max Planck Institut für Kernphysik in Heidelberg as Alexander von Humboldt fellow. He is currently member of the Faculty of the Politecnico of Milano as assistant professor. His research interests are focused on investigation of ultrafast molecular processes and characterization of attosecond electron dynamics by coincidence measurements of charged particles.

PLACE PHOTO HERE

F reek Kelkensberg In 2006 he obtained his Masters degree in Applied Physics from Delft University of Technology on the development of single-photon nano-LEDs. At the FOM-Institute AMOLF he is currently working on his PhD-thesis on the application of attosecond pulses to study time-resolved electron dynamics.

PLACE PHOTO HERE

F elipe Morales received his Ph.D from the Universidad Autónoma de Madrid in 2009 where he brought his computer science background to bear on the large- scale computational modelling of the interaction of atoms and molecules with laser fields. In 2010 he joined the theory group at the Max-Born Institute (MBI) in Berlin as a visiting scientist. Later that year he was awarded a post-doctoral fellowship by the Spanish Ministry of Education to continue his work at MBI. His current research interests include multiphoton single and double ionization of atoms and molecules, attosecond physics and strong fields, with a focus on accurate quantum simulations through the use of high performance computing.

PLACE PHOTO HERE

H e obtained his Masters degree in Theoretical Chemistry from the Universidad de Antiqoquia, Colombia in 2007 investigating the quantum control of Hooke's atom perturbed by laser pulses. In 2008, he received his second Masters degree in Theoretical Chemistry and Computational Modeling from the Universidad Autónoma de Madrid for studying the dynamics of the dissociative photoionization of H_2 molecules with ultra-short laser pulses. Currently, he is working on his PhD thesis in the field of the theoretical description of the ionization of H_2 molecules by ultra-short XUV laser pulses and infrared probe pulses.

PLACE PHOTO HERE

H e received his PhD in 1986 in the Universidad Autonoma de Madrid and is currently the chair of the Department of Chemistry and the director of its theory group in the same university. He is also the coordinator of the European COST Action "Chemistry with ultrashort pulses and free electron laser". His research interests include ultrafast molecular processes induced by lasers, molecular reactivity on metal surfaces and fragmentation dynamics of clusters and biomolecules induced by collisions with multiply charged ions.

P rof. Dr. Marc Vrakking obtained his Phd in 1992 from the University of California at Berkeley (USA). He recently joined the Freie Universität Berlin and the Max Born Institute as the new director of Division A, having previously been a groupleader at the FOM Institute for Atomic and Molecular Physics (AMOLF) in Amsterdam, the Netherlands. His research concentrates on the application of attosecond laser pulses to study time-resolved electron dynamics and the use of XUV/x-ray free electrons lasers (FLASH, LCLS) to develop diffraction-based techniques for studying time-resolved molecular re-arrangement and dissociation. He was the coordinator of the FP6 EU Marie-Curie Research Training Network 'XTRA' (Ultrashort XUV Pulses for Time-Resolved and Non-Linear Applications), and presently coordinates FP7 Initial Training Network 'ATTOFEL' (Ultrafast Dynamics using ATTosecond and XUV Free Electron Laser Sources). He also coordinates a Marie Curie Industry-Academia Partnership Program, where co-development with industrial parties is pursued to develop the driver lasers of the future for attosecond research.